Additive Manufacturing Letters 14 (2025) 100305

Contents lists available at ScienceDirect

Additive Manufacturing Letters

journal homepage: www.elsevier.com/locate/addlet

Short Communication

Processing of Thermoelectric Fe_2VAl Heusler-compounds by laser powder bed fusion: From single scan tracks to bulk material

M. Delcroix *, G. Roy, C. van der Rest, V. Marchal-Marchant, P.J. Jacques

UCLouvain, Institute of Mechanics, Materials and Civil Engineering (IMMC), Materials and Process Engineering (IMAP), Réaumur, Place Sainte Barbe 2, 1348 Louvain-la-Neuve, Belgium

ARTICLE INFO

Keywords:
Heusler
Thermoelectric
Additive manufacturing
Single scan track
Crack defects

ABSTRACT

In the present study, the n-type Fe_2 $VAl_{0.9}$ $Si_{0.1}$ was printed by laser powder bed fusion (L-PBF) for the first time. This work highlights the complexity of processing non-metallic materials by L-PBF and the need for advanced optimization strategies. A Single Scan Tracks (SSTs) analysis was conducted as usually done for materials newly processed by L-PBF as well as a top-down approach based on printing parameters of stainless steel. Process parameter sets based on SST analysis led to overheating while the stainless-steel-based strategy successfully produced bulk samples. Printed samples transitioned rapidly from cold defects (i.e. lack-of-fusion) to overheating as the printing parameters were varied. Moreover, high density samples were printed with parameters that would produce insufficient melting in the case of SSTs. Successive parallel tracks were printed and revealed a transition from unmelting to balling to continuous densification, demonstrating the critical role of heat accumulation. The microstructure of printed samples was analyzed, and their thermoelectric properties were measured. Transverse cold cracks, perpendicular to the scanning direction were observed. Statistical analysis on SST demonstrated that these cracks were insensitive to laser parameter variations, significantly decreasing the thermoelectric performance of bulk samples.

1. Introduction

Thermoelectric (TE) materials, which can convert waste heat to electrical energy, have gained some interest in the past few years due to increasing concerns about energy sustainability. This energy conversion is based on the Seebeck effect, which is the ability of a material to produce an electrical potential when submitted to a given temperature gradient. This ability is quantified and expressed by the Seebeck coefficient $S = \frac{dV}{dT}$ [V/K]. The performance of TE materials is usually expressed by means of a dimensionless figure of merit $ZT = \frac{S^2\sigma}{\kappa}T$, with σ being the electrical conductivity of the material, κ its thermal conductivity and T the absolute temperature. The efficiency of the conversion increases monotonically with the ZT-value. The numerator of Z is called the power factor $PF = S^2\sigma$ [W/(m K^2)] and describes the energy density of the conversion.

Among thermoelectric materials, the Full-Heusler compound Fe_2VAl is a good candidate for large scale applications due to the abundance and the relatively low cost of its constitutive elements. The Fe_2VAl-related system is well known to exhibit high power factor. Nishino et al. (2004) reported power factors up to 5.5 mW/m K^2 in the case of $Fe_2VAl_{0.9}Si_{0.1}$ compound [1] and more recently, Garmroudi et al. (2021) measured an extremely high power factor close to 10.3 mW/m K^2 for the $Fe_2V_{0.95}Ta_{0.05}Al_{0.9}Si_{0.1}$ compound [2]. While the ZT value of the Fe_2VAl compound remains limited compared to state-of-the-art thermoelectric materials, mainly due to its high thermal conductivity (10–30 W/(m K)), recent publications have reported significant breakthroughs. For instance, Fukuta et al. (2022) achieved a ZT of 0.37 at 400 K by reducing the thermal conductivity using high-pressure torsion processing [3]. More recently, Garmroudi et al. (2024) pushed the performance further, reaching a ZT of 0.5 at 295 K in a $Fe_2V_{0.95}Ta_{0.1}Al_{0.95}/Bi_{0.9}Sb_{0.1}$ composite produced by liquid-phase sintering [4].

Even if these types of compounds are relatively cheap and present attractive TE properties, manufacturing of a large number of thermoelectric generators (TEGs) coupling numerous small pieces of TE materials is still challenging. To solve this bottleneck in TEG development, larger easiness could be provided by Laser Powder Bed Fusion (L-PBF) directly printing net-shape TE legs. Moreover, it would allow to increase complexity of the TEGs with shape optimization or even topology optimization to improve conversion efficiency [5–7]. Additive manufacturing of TE material with L-PBF technique is a quite emerging topic with El Desouki et al. (2015) who studied Bi_2Te_3 laser processing [8,9]. In an other study, Mao et al. (2017) succeeded to

* Corresponding author.
E-mail address: mathieu.delcroix@uclouvain.be (M. Delcroix).

https://doi.org/10.1016/j.addlet.2025.100305
Received 24 April 2025; Received in revised form 3 July 2025; Accepted 13 July 2025
Available online 24 July 2025

Table 1
Chemical analysis of GA and crushed powders used for the L-PBF.

	Fe [at %]	V [at %]	Al [at %]	Si [at %]	Mn [at %]	Ni [at %]
GA powder	50.3	23.94	25.15	0.3	0.1	0.22
Crushed powder	49.87	24.81	22.72	2.35	–	0.22

print n-type $Bi_2Te_{2.7}Se_{0.3}$ with a large figure of merit (ZT) value of 0.84 around 400 K measured perpendicularly to the building direction [10]. Shi et al. manufactured porous p-type BiSbTe by L-PBF that has a higher ZT value than the Spark plasma Sintered (SPS) bulk sample [11]. Yan et al. (2018) broadened the list of printable TE materials by L-PBF with $CoSb_{0.85}Te_{0.15}$ skutterudite [12] and ZrNiSn Half-Heusler compound [13] with crushed powders thanks to Self-Propagation High-Temperature Synthesis (SHS). Baudry et al. (2023) recently succeeded to print n-type SiGe with a density higher than 96%. However, the samples exhibited cracks that significantly reduce their electrical conductivity [14].

While Fe_2VAl printing by L-PBF has not been reported yet in the literature, Gomell et al. (2021) have already investigated Surface Laser Remelting (SLR) of stoechiometric Fe_2VAl with a L-PBF system [15,16]. Their research focused on the influence of the ultra fast heating and cooling rate of the process on the microstructure and its influence on the TE properties of the compound. It was shown that SLR created elongated grains with low misorientation between them, reducing the resistivity of the grain boundaries compared to high misorientation [15]. The size of the grains measured parallel to the surface was around 1 μm, which is smaller than the expected phonon mean free path (~2.4 μm) and could lead to the reduction of the lattice thermal conductivity of the material. It was also shown that V tends to segregate with N (coming from alloying and sample processing) at the grain boundaries, leading to slight composition heterogeneity. This study concluded that the decrease of thermal conductivity and electrical conductivity lead to an increase of 6% of the TE performance for the selected process parameters [16].

In the present study, $Fe_2VAl_{0.9}Si_{0.1}$ was printed by L-PBF for the first time. Since no previous study was available in literature, a Single Scan Tracks (SSTs) strategy was conducted as usually done for materials newly processed by L-PBF [17]. From top-view and cross-sections analysis of the SSTs, a model was built to select combinations of theoretical parameters to reach high density parts. A top-down approach was also used based on printing parameters of stainless steel. Finally, the microstructure of printed samples was analyzed and their thermoelectric properties were measured.

2. Materials and experimental procedure

2.1. Materials

Two different types of powders were used. The first one was a Fe_2VAl gas atomized (GA) spherical powder sieved below 45 μm. The d_{10}, d_{50} and d_{90} were 9, 20 and 39 μm, respectively. The second powder was obtained by crushing an ingot of $Fe_2VAl_{0.9}Si_{0.1}$ and then sieving below 63 μm and 45 μm, successively. The two powder cuts were characterized by granulometry. The powder sieved below 45 μm had d_{10}, d_{50} and d_{90} values of 7, 22 and 47 μm, respectively. The powder sieved between 45 μm and 63 μm had d_{10}, d_{50} and d_{90} values of 42, 57 and 79 μm, respectively. The final powder consisted in a mix of 70 wt % of powder sieved below 45 μm and 30 wt % sieved between 45 μm and 63 μm. The coarser powder was added to increase the flowability of the mix. Table 1 shows Inductively Coupled Plasma Spectroscopy (ICP) analysis performed on both powders. The compositions of the two powders are slightly different since the crushed powder was Si-doped. This is supposed to have a minor effect on processability of the material by L-PBF.

2.2. L-PBF manufacturing and characterization

All samples were manufactured with a ProX200 L-PBF machine from 3DSystems equiped with a laser with a wavelength of 1070 nm, a maximum power of 273 W and a spot diameter of 75 μm, working under argon atmosphere with an oxygen content maintained below 800 ppm. The powder layer thickness was kept constant at 45 μm for the whole study and the rotation of the scanning vector was 67° between each layer. Since no previous study has been published about L-PBF of Fe_2VAl, two strategies were tested to optimize the printing parameters. The first approach was some kind of a "bottom-up" strategy starting from single scan tracks (SSTs) analysis. The SSTs were built on a thin Fe_2VAl plate previously printed on a stainless steel circular plate (20 mm diameter) to avoid mixing of substrate material and the zone of interest on the printed samples. The 1 mm thick Fe_2VAl plate was printed based on parameter advised by the manufacturer for stainless steel adjusted for a layer thickness of t = 45 μm (laser power P = 190 W, scanning speed v = 1400 mm/s, hatch space HS = 50 μm). The second approach consisted in tuning these adjusted parameters provided by printer manufacturer for processing stainless steel powder. Indeed, stainless steel and $Fe_2VAl_{0.9}Si_{0.1}$ have roughly the same thermal properties (thermal expansion coefficients, thermal conductivities at ambient temperature and melting temperatures). A test batch of 14 mm × 4 mm × 4 mm blocks was built to investigate the process window around these parameters. The dimensions of the blocks were chosen to match the requirements for Seebeck and electrical conductivity measurements with SBA 458 Nemesis equipment from NETZSCH. Measurements were carried out during both heating and cooling to ensure the thermal stability of the tested samples. Since no significant differences were observed, only the heating measurements are presented. A square block with a 10 mm × 10 mm base and a 3 mm thickness was also printed to measure the thermal conductivity with a laserflash LFA 467 from NETZSCH.

Microstructure characterization was carried out by Scanning Electron Microscopy (ZEISS FEGSEM Ultra 55) and 3D optical Microscopy (KEYENCE VHX-7000). For cross-section imaging, the samples were polished with SiC paper down to 1200 grit and diamond suspension solution of 6 μm to 1 μm, and final polishing step using colloidal silica suspension of 0.25 μm (OP-S).

Sintered sample was used for thermoelectric performance comparison. It was pressed using an adapted graphite die and sintered at 1373 K for 1 h. The heating rate was 10 K/min and the applied load was 40 MPa. The powder used for sintering was the same crushed powder as for L-PBF sieved below <45 μm.

3. Optimization of the L-PBF process parameters

3.1. Approach I : Single scan tracks analysis

The single scan tracks (SSTs) approach consisted in analyzing the morphology and the shape of a single laser scanning track on a single layer of powder as a function of laser power P and the scanning speed v. The width of the stable and continuous track presenting a wetting angle between 50° and 100° is measured in order to determine the adequate distance between successive tracks, also called the hatch space HS. This approach enables to estimate a set of process parameters (P, v, HS) on the basis of a SST. [17]

Fig. 1 summarizes the results of the SST analysis and shows the different SST types as it is commonly reported in the literature [14,18].

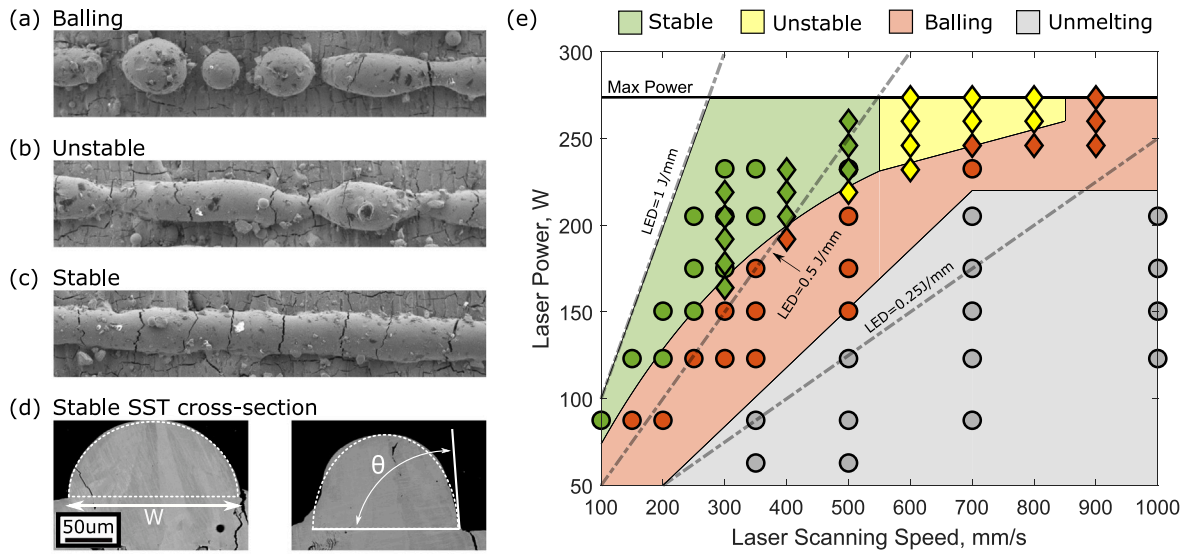

Fig. 1. (a–c) Top-view SEM micrographs of the different modes of SST. (d) Typical SEM micrographs of cross-sections used for width measurements. (e) SST mode map. Circles (resp. Diamonds) represent samples built with spherical (resp. irregular) powder.

The laser power P and laser scanning speed v were varied over wide ranges to observe their influence on the SST stability. The results of these observations are synthesized on a map in Fig. 1(e). Different levels of linear energy density, defined as LED [J/mm] = $\frac{P\ [\mathrm{W}]}{v\ [\mathrm{mm/s}]}$ are added on the map. It can be observed that the transitions between the different modes are similar for both types of powders (i.e. gas atomized and crushed). This suggests that the morphology of the powder has no significant influence on the process. For LED levels lower than ~0.25 J/mm, there is no melted material remaining on the substrate. It means that the depth of the meltpool was not sufficient compared to the powder layer thickness. For slightly higher LED, droplets of melted materials are observed along the SST direction (Fig. 1b). This phenomenon is know as "balling" in the literature and causes lack-of-fusion (LoF) in the printed parts. A minimum LED of ~0.5 J/mm is required to produce a continuous and stable (i.e. constant width) SST, as depicted by Fig. 1(c), suitable for bulk samples printing. At high P and v > 500 mm/s, some SSTs were also continuous but are considered as unstable because there are some neckings along the track (Fig. 1b). This mode of SST would also produce LoF in a printed part. Commonly, at high LED levels, keyhole mode is also observed. It was not the case here since generally, the supporting printed layers were too damaged to clearly observe the meltpool depth. Nevertheless, that keyhole mode could be present for LED values higher than 1 J/mm.

In the case of bulk samples, an adequate hatch spacing has to be selected to ensure sufficient overlapping of the meltpools. The overlapping rate can be defined as $\phi = 1 - \frac{HS}{W}$, where W is the meltpool width measured as depicted in Fig. 1(d). Commonly, ϕ values between 0.25 and 0.5 are necessary according to the literature [17,19,20]. Fig. 2(a) shows the SST width measurements as a function of the LED. Only the continuous and stable SSTs were considered here (LED > 0.45 J/mm). It is shown that the track width increases with an increasing LED.

By fixing ϕ, the Volumic Energy Density, defined has $VED = \frac{P}{vHSt} = \frac{LED}{t(1-\phi)W}$, can be computed for a part based on the LED only, since the powder bed thickness t is fixed in this study. Fig. 2(b) shows the VED computed based on SST width measurements for the two extreme cases of ϕ suggested here above. It is shown that depending on (P, v, ϕ), the HS should range from 60 μm to 170 μm with a VED ranging from 82 J/mm^3 to 193 J/mm^3.

Numerous trials to print bulk samples based on the results of the SST strategy were attempted, with largely varying parameters : P spanning from 164 W to 232 W, v from 250 mm/s to 500 mm/s and ϕ from 0.25 to 0.50, corresponding to a VED ranging from 82 J/mm^3 to 200 J/mm^3. Nevertheless, all of the tested sets of parameters based on the SSTs analysis led to high overheating defects. This means that the classical SST approach for determining printing parameters is not suitable for $Fe_2VAl_{0.9}Si_{0.1}$. Indeed, its brittleness makes it very sensitive to thermal stresses and then thermal history of the sample during the process. This thermo-physical profile adds some constraints on the process parameters that are not taken into account by this approach. This suggests that there is no (P, v, HS) process window where the 3 following conditions are full-filed : the SST is continuous, the overlapping of two consecutive tracks is sufficient and there is no overheating when printing several tracks side by side. The SST approach, which is mostly based on geometrical criteria, imposed a minimal VED that unavoidably induces overheating.

3.2. Approach II : Case-inspired optimization

Since preliminary tests based on standard parameters provided by the L-PBF printer manufacturer for stainless steel (P = 191 W, v = 1400 mm/s, HS = 50 μm) were encouraging, a batch of bulk samples was printed to explore the process window around these parameters. The HS was kept constant at 50 μm. All the tested sets of parameters are summarized in Appendix.

Fig. 3(a) summarizes the general quality of the printed samples on a process map. This map suggests that there is a critical VED, slightly above 60 J/mm^3 that separates two main defect zones. Above this limit, overheating starts to appear, bringing strong warping of the samples (Fig. 3(d)). For even higher VED (>80 J/mm^3), overheating is so large that the samples are totally detached (Fig. 3(c)). Below a VED of 60 J/mm^3, in the low P and high v region, the meltpool depth becomes small compared to the layer thickness. Lots of lack-of-fusion defects appear (Fig. 3(e)). If the VED is further decreased, the cohesion between the printed layers is so weak that the part totally collapses at the end of the printing (Fig. 3(b)). The same kind of defects is observed for the low P and low v zone. For the high P and high v zone, heat accumulation occurs at the sample corners where scanning vectors are shorter, leading to warping defects of these corners. At the center of the processing map, there is a narrow "Trade-Off" zone where the VED is low enough to avoid overheating but high enough to ensure a sufficient melting depth. The parts printed in this zone are "net-shape" without any macroscopic defects (Fig. 3(f)). It might be highlighted that the typical building rate in the "Trade-Off" zone is 3–3.5 mm^3/s. A Fe_2VAl-based thermoelectric generator counts roughly 36 legs with

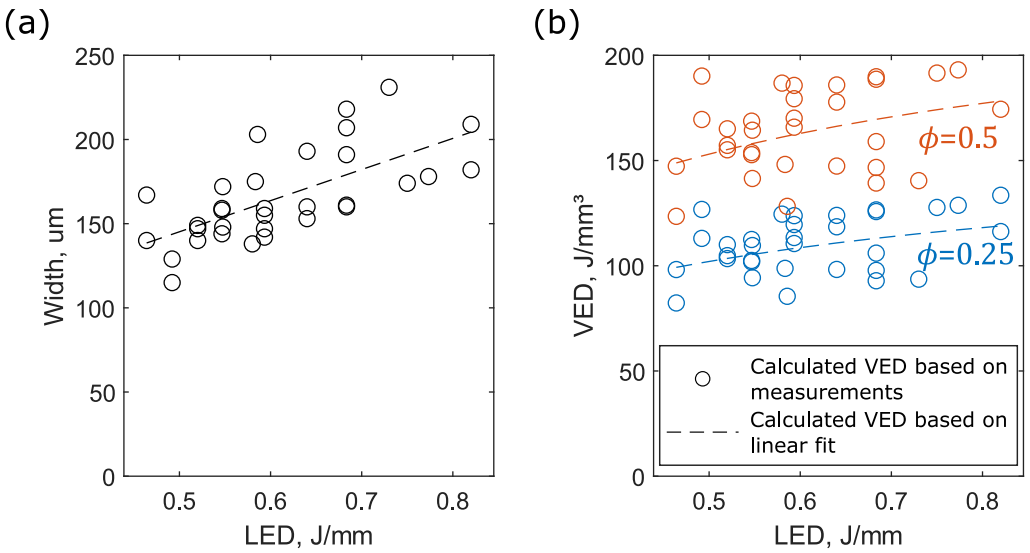

Fig. 2. (a) Measured SST width, W, as a function of the LED of the laser. (b) Volumic Energy Density (VED) needed to print a volume sample considering $HS = (1 - \phi)W$, as a function of the LED of the laser.

a volume between 12 and 25 mm^3 each [21,22]. This demonstrates that LPBF could produce enough net-shape legs to assemble 20–30 TEGs per hour. Therefore, LPBF might be highly competitive with typical machining techniques, while also offering the advantage of shape-optimized geometries and reduced material losses.

3.3. Comparison of procedures of the process parameters optimization

Both optimization approaches presented above were constrained by overheating issues. On the one hand, it was determined from approach II that for VED higher than ~60 J/mm^3, the printed part exhibits destructive warping defects due to overheating. On the other hand, all attempts to print parts based on approach I failed due to overheating. Indeed, approach I suggested that a minimum VED of 82 J/mm^3 is required to print parts with sufficient overlapping of successive stable and continuous meltpools. Approach II determined experimentally that 60 J/mm^3 was the VED upper limit and demonstrated that approach I was not sufficient to identify an ideal process parameter. Moreover, both approaches suggest that printed parts will inherently exhibit LoF porosities. In metal additive manufacturing, parts typically evolve from LoF porosities to dense parts and then to keyhole porosities as the VED increases. Since porosity negatively impacts mechanical properties, the upper limit of VED is usually set by the onset of keyhole formation. For instance, in the case of 316L stainless steel, Eliasu et al. (2021) demonstrated that LoF-related porosity decreases when VED increases from 28 J/mm^3 to 67 J/mm^3, remains low between 67 J/mm^3 and 111 J/mm^3, and keyhole porosity appears only above 142 J/mm^3 [23]. This means that the defect evolution spans a wide VED range for 316L. In contrast, $Fe_2VAl_{0.9}Si_{0.1}$ has a notably low VED upper limit due to its specific thermophysical properties. As a result, the processing window is significantly narrower, restricting the usable VED range to a small area where LoF porosity cannot be avoided.

The printed samples from approach II in the "Trade-Off" zone had a low LED (<0.15 J/mm) that would produce unmelted SSTs mode according to approach I (Fig. 1). In order to evaluate how successive scan tracks interact with each other, successive parallel tracks were printed directly on the top of a 4 mm thick block built with the same parameters (P,v,HS). Fig. 4 depicted the morphology and the height profiles of samples presenting 1 to 30 successive tracks.

It can be seen in Fig. 4 that for 1 SST, there is no melted material on top of the block with P = 164 W and v = 1200 mm/s, as expected from Fig. 1. It means that the LED is too small to melt the whole thickness of powder. After 5 consecutive tracks, some melted material remains on the surface of the previous layer but generates balling. The height of the balling droplets is higher than the layer thickness (t = 45 μm). These large droplets could be due to accumulation of melted material from the successive neighboring tracks. Indeed, even if the melting of the first tracks is not deep enough to induce sticking to the substrate, some melted material could remain on top of the powder layer. This melted material could be partially remelted and sticked to the surface by the following tracks. The same phenomenon is observed for 10 successive tracks, but a transition to a more continuous mode starts to appear for the last printed tracks. From 20 tracks on, a transition from balling to continuous mode can be clearly observed. In the continuous zone, the measured height (~60 μm) seems to be more coherent with the powder layer thickness but is still thicker. This shows how parts can be printed even with parameters that corresponds to "unmelting" or "balling" modes from the SST mode map. It suggests that heat accumulation in a single layer is much more significant than heat accumulation between successive layers. Aside from heat accumulation, the balling to continuous transition could be partially explained by the accumulation of material already melted. Indeed, since the balling phenomenon appears to minimize the free surface area of the meltpool [17], the presence of a neighboring track could decrease the free surface area of the new meltpool and stabilize it. To the authors' best knowledge, this unmelting-to-balling-to-continuous mode transition was never investigated or exposed properly in the literature. Further work is needed to better understand this phenomenon, which might be a relevant factor for processing other novel materials that are highly sensitive to heat accumulation.

4. Microstructures and properties of printed samples

4.1. Transverse cracks in SST

It has to be pointed out that all top-view observations of SSTs exhibit cracks that are oriented perpendicularly to the scanning vector as shown in Fig. 5. These transverse cracks (T-cracks) were largely described by Lee et al. and were associated to high thermal stresses parallel to the scanning direction. As the melt pool solidifies, it remains significantly hotter than the underlying substrate and experiences increasing tensile stress during cooling. When this stress exceeds the material's yield strength, cracks initiate and propagate. According to Lee et al. the spacing between cracks is influenced by the process parameters, particularly the laser scanning speed [24].

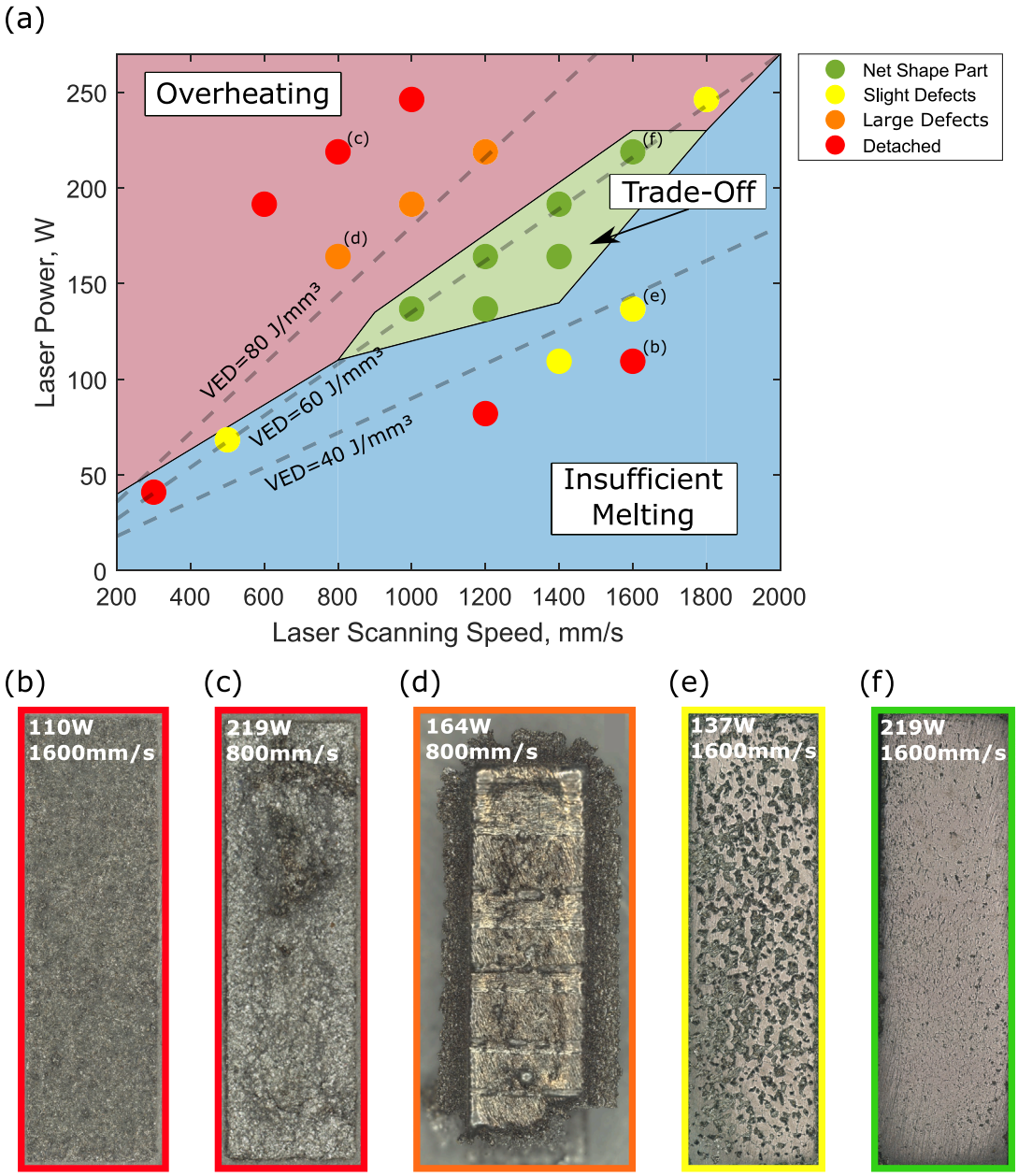

Fig. 3. (a) Printability map of bulk samples of $Fe_2VAl_{0.9}Si_{0.1}$ at constant HS of 50 µm. (b–d) Light micrographs of the top surface of different type of samples with major defects. (e–f) Polished cross-section at the middle of the samples resenting slight defects.

To evaluate the impact of the lasing parameters (v and P) on the cracking behavior, distances (d_{i-c}) between successive cracks were measured on the stable and continuous tracks printed with crushed powder. The length of each measured SST was ~4 mm. One-way Analysis of Variance (ANOVA) was then used to assess any significant mean d_{i-c} ($\overline{d_{i-c}}$) difference between SSTs, following the methodology given in [25]. The aim of this analysis was to check if the process parameters (P or v) have an influence on $\overline{d_{i-c}}$. For the validity of the method, each dataset must be normally distributed and their variances need to be equivalent. A Shapiro–Wilk test was first applied on each set of SSTs measurements to verify that d_{i-c} values were normally distributed. Among 10 measured SSTs, one was rejected (p-value = 0.042). A Bartlett test was then applied to assess the equivalence of the variances. The null hypothesis $H^0 : \sigma(d_{i-c})_j = \sigma(d_{i-c})_k = \cdots$ was not rejected with a p-value of 0.80. Groups were formed such that only one process parameter is varied : constant v - different P or constant P - different v, as synthesized in Table 2. The null hypothesis to be tested was then $H^0 : \overline{d_{i-c\,j}} = \overline{d_{i-c\,k}} = \cdots$. This H^0 is never rejected because the p-value is greater than 0.05 for all the tested groups. This means that there is no evidence that $\overline{d_{i-c}}$ significantly differs for the different SSTs. This suggests that, within the investigated range, v and P have no significant influence on the cracking behavior. It implies that the cracking problem could not be solved by simple optimization of the considered process parameters, which contrast with the findings presented by Lee et al. in [24]. This constitutes a first obstacle for printing of crack-free parts of $Fe_2VAl_{0.9}Si_{0.1}$.

4.2. Density

The density of the printed samples was measured on the center of the samples by light microscopy. The Archimede's method was not considered since the numerous cracks could bias the discrimination between close and open porosities. The measurements are summarized

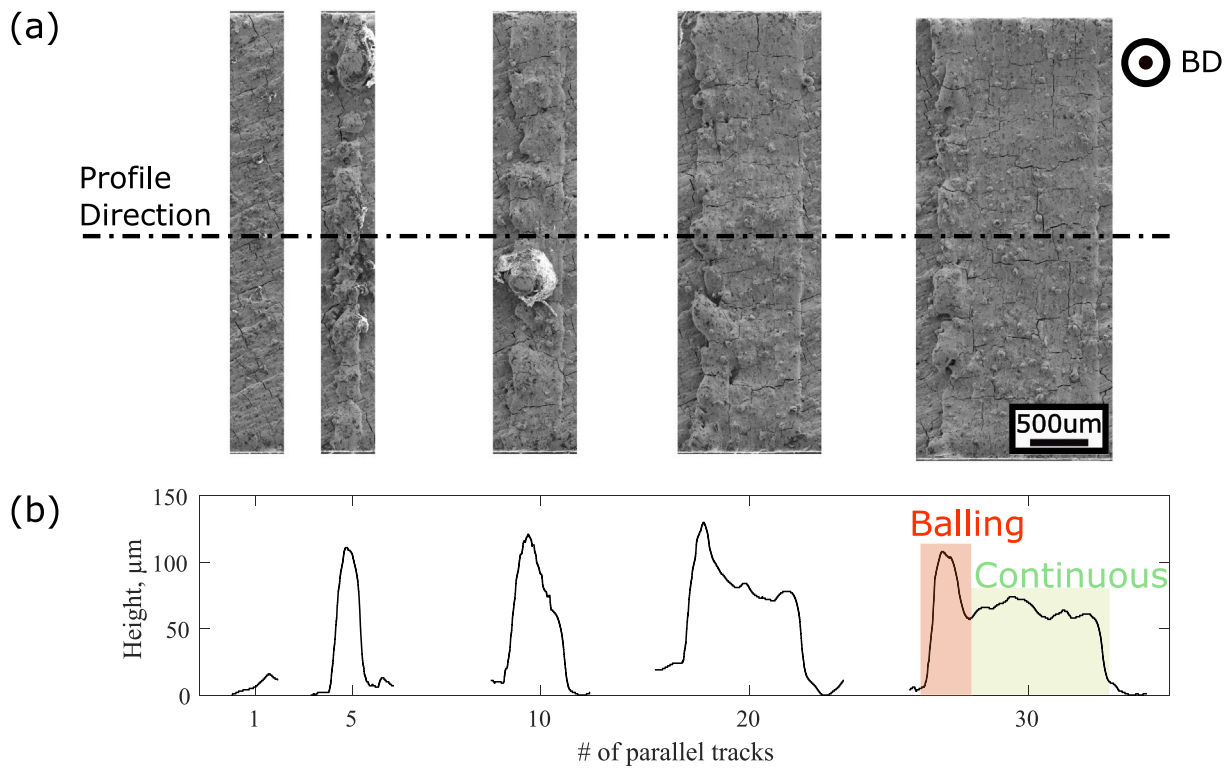

Fig. 4. (a) Top-view SEM micrograph of successive scan tracks on top of a printed volume sample. The laser power was 164 W and the scanning speed was 1200 mm/s. (b) Corresponding average height profile, based on measurement of 60 parallel profiles spaced by 50 µm obtained with 3D light microscopy. The scanning tracks were successively deposited from the left to the right.

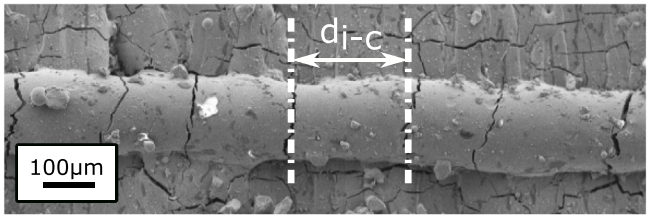

Fig. 5. SEM (secondary electrons) of a SST with d_{i-c} indicating two successives cracks.

Table 2
Synthesis of the results of the ANOVA analysis. For each analysis, Parameter 1 is kept constant and Parameter 2 is swept in order to perform one-way ANOVA.

Parameter 1	Parameter 2	$\overline{d_{i-c}}$ [µm]	$\sigma(d_{i-c})$ [µm]	H^0 p-value
v = 300 mm/s	P = 164 W	187	78	0.66
	P = 178 W	198	74	
	P = 192 W	193	63	
	P = 205 W	217	79	
v = 400 mm/s	P = 205 W	219	76	0.88
	P = 219 W	219	69	
	P = 232 W	229	56	
v = 500 mm/s	P = 232 W	197	76	0.46
	P = 260 W	216	69	
P = 205 W	v = 300 mm/s	217	79	0.92
	v = 400 mm/s	219	75	
P = 232 W	v = 400 mm/s	229	56	0.17
	v = 500 mm/s	197	76	

in Fig. 6. As expected, samples from the "Insufficient Melting" zone have a very low density since cohesion between layers and meltpools is low. Then, pieces of materials could be torn from the sample either during the printing process or during the polishing step. In the "Trade-Off" zone, most of the samples show densities higher than 90% with a peak value of 96.6% for P = 164 W and v = 1200 mm/s. The highest measured density was 97.3% on the only sample remaining from the "Overheating" zone where there are less LoFs defects. Nevertheless, that high value does not take into account the missing broken corners of this sample due to warping defects.

4.3. Microstructure and defects

Fig. 7 synthesizes different micrographs of the sample processed with $P = 191$ W and $v = 1400$ mm/s, which is representative of samples from the "trade-off" zone described in Fig. 3. Fig. 7(a) confirms the presence of numerous cracks in the printed samples, as expected from SSTs analysis. In a cross-section perpendicular to the building direction (BD), there is no preferential orientation for these cracks. This could be related to the fact that cracks are perpendicular to the scanning vectors that are rotated by 67° between each layer. Grains observed within this plane (Fig. 7(b)) seem to be relatively small with a characteristic size roughly below 10 µm. In Fig. 7(c), an irregular porosity with partially melted powder is shown. It could be related to lack-of-fusion defects that are expected in that sample since the VED is low [26]. Moreover, there are many channels with unmelted powder inside such as depicted by Fig. 7(d). These could also be powder pockets due to lack-of-fusion or simply thick cracks filled with powder during the process.

In a cross-section parallel to BD (Fig. 7(e)), the defects seem to be preferentially oriented parallel to the building direction (BD). According to the SST analysis, the cracks appear perpendicularly to the scanning vector, thus, parallel to BD. Looking at Fig. 7(f), grains are columnar and are also oriented parallel to the building direction. Fig. 7(g) shows large cavities (~100 µm) that exhibit cleavage patterns indicating brittle fracture. It can be assumed that these cavities are not lack-of-fusion defects (LoF) but small pieces of material that were scratched away during the cutting or the polishing of the sample. This

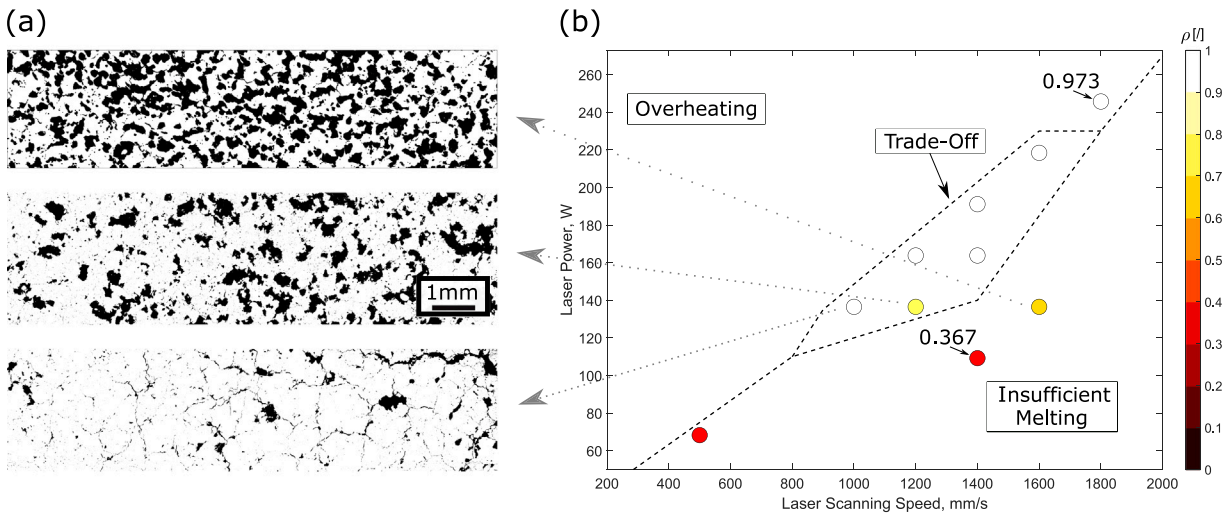

Fig. 6. (a) Thresholded light micrographs used for relative density measurement of the printed samples. (b) Map of the relative density of the printed samples. Maximal and minimal values are highlighted. Details are available in Appendix.

is corroborated by the fact that the cleavage patterns are oriented in the same direction than the crack propagations, parallel to BD. Finally, Fig. 7(h) shows a porosity that could be a LoF since there is no sign of brittle fracture in that case. Above that cavity, there are some small particles that could correspond to unmelted powder, as presented in Fig. 7(d).

4.4. Thermoelectric properties

The electrical conductivity and the Seebeck coefficient of the printed samples were measured. Fig. 8 shows these measurements at room temperature for the different manufacturing parameters.

The Seebeck coefficient of the printed samples exhibits only slight variations at room temperature. Indeed, the measured values range for −127 to −111 μV/K (Fig. 8(a)) with a mean value of −120μV/K. Seebeck coefficient is mainly dependent on the composition and should not be affected by defects such as cracks or lack-of-fusion. However, slight Al evaporation due to high energy density of the laser could change the material composition and affect the Seebeck coefficient, which can be very sensitive to composition deviation [27]. Moreover, the accuracy on the measurement of the equipment (SBA 458 Nemesis from NETZCH) is ±7% and could partially explain this slight variation. For the electrical conductivity, a significant difference can be noticed between samples in the "Trade-Off" zone and in the "Insufficient Melting" zone (Fig. 8(b)). Samples with a lot of lack-of-fusion defects have a lower electrical conductivity due to their lower density, as explained for Fig. 6. Samples in the "trade-off" zone have a fairly equivalent electrical conductivity. This observation is consistent with crack measurements performed on single scan tracks in Section 4.1. Indeed, if the process parameters do not influence the cracking behavior, then net-shape samples from the "trade-off" zone should exhibit a similar crack density, leading to comparable electrical conductivity.

TE properties were also measured at different temperatures as depicted in Fig. 9 for some samples. Measurements made on sintered reference sample are added for comparison.

There is no significant difference in the Seebeck coefficient between the different printed samples over the tested temperature range. The absolute Seebeeck coefficient value of the printed samples is slightly higher than for the sintered reference sample at higher temperature. As expected, due to the large crack density, the electrical conductivity of the printed samples is drastically lower than this reference sample by almost two orders of magnitude. The two samples printed with parameters in the "trade-off zone" (218 W–1600 mm/s and 136 W–1000 mm/s), as defined in Fig. 3, have a higher electrical conductivity than the one with lack-of-fusion defects. The thermal conductivity of the printed sample is around ≈6 W/m K. This small value when compared to the sintered sample can also be explained by the large density of cracks. However, relative drop of thermal conductivity does not compensate the drop of electrical conductivity in the dimensionless figure of merit ZT, which is smaller for the printed samples. It has to be mentioned that the computed ZT is a rough estimation since S and σ are measured perpendicularly to κ. Indeed, crack defects are oriented parallel to BD so that transport properties measurement could be different depending on their direction regarding the building direction.

Overall, it can be concluded that the process parameters, over the tested range, do not have a significant influence on the Seebeck coefficient or electrical conductivity. If the drop of electrical conductivity is mainly explained by the presence of cracks, the latter conclusion is in agreement with previous analysis that demonstrates (based on ANOVA) that the process parameters, in the tested range, have no significant influence on cracks inter-distance in SSTs.

5. Conclusion

In this study, Fe_2VAl Heusler compound was printed by L-PBF for the first time. As a first step, a single scan track analysis was carried out and highlighted the following elements :

1. Either with a spherical or irregular powder, a minimum LED of ~0.5 J/mm is necessary to produce a continuous and stable SST.
2. All the SSTs show transverse micro-cracks spaced by ~200 µm. It was assessed by ANOVA that this inter-crack distance is similar for every set of parameters (laser power and scanning speed) over the tested range, suggesting that these defects cannot be mitigated by simple optimization of the laser scanning speed or power.
3. Analysis based on the SST width shows that a minimal VED of 82 J/mm^3 is required to ensure sufficient overlapping of successive meltpools. Unfortunately, this minimal value is still too high and the printed samples suffered from overheating, leading to strong warping defects and decohesion of parts from the plate.
4. There is no set of parameters that can simultaneously fulfill the following conditions : (i) the SST is continuous, (ii) the overlapping of the meltpool is sufficient to avoid lack-of-fusion defects and (iii) the VED is low enough to prevent overheating.

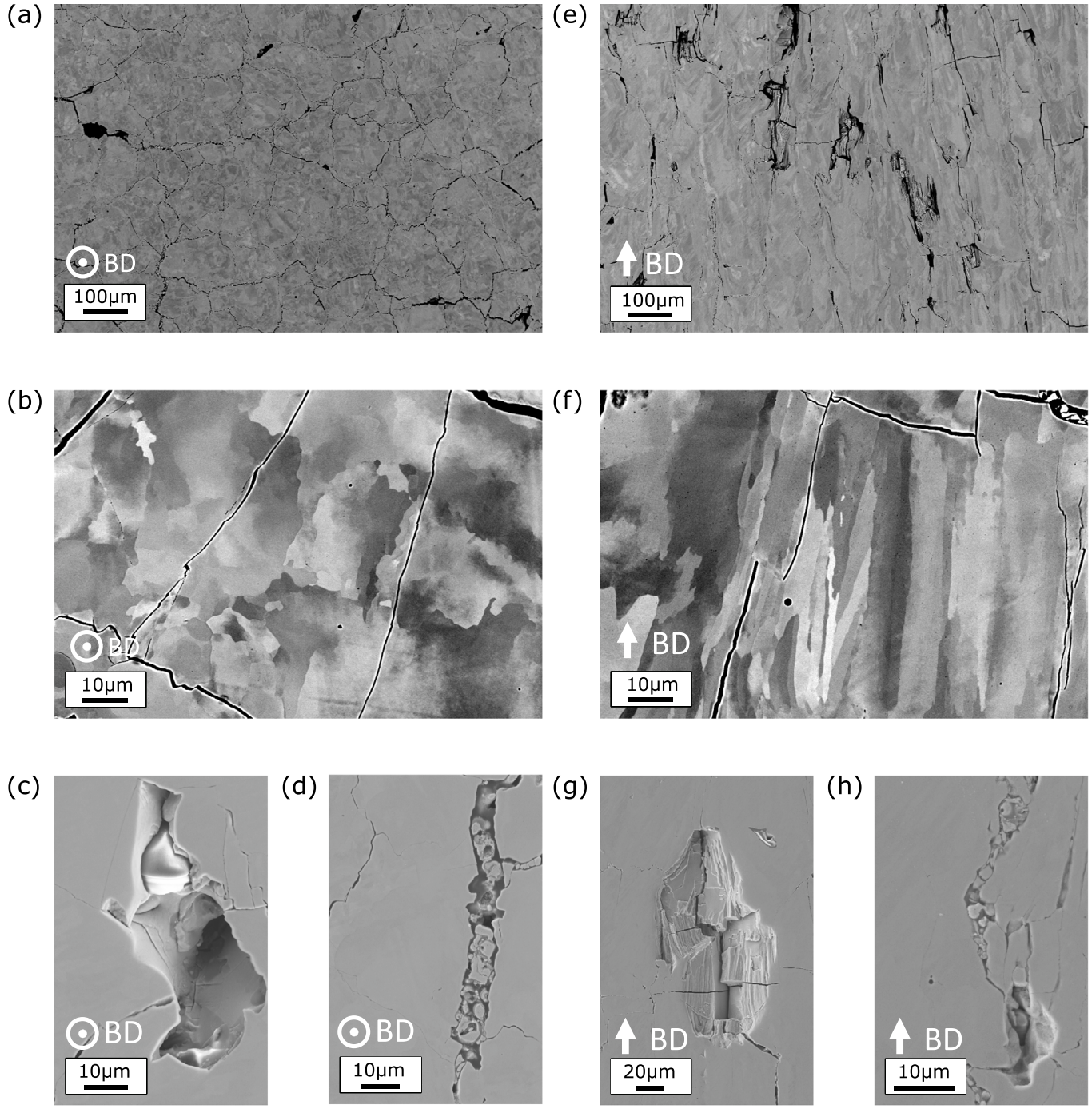

Fig. 7. SEM micrographs of a printed sample withP = 191 W, v = 1400 mm/s and HS = 50 µm. Micrographs (a) to (d) are taken perpendicular to the building direction (BD), while (e) to (h) are taken parallel to the BD. Micrographs (c), (d), (g) and (h) correspond to a secondary electron contrast. The other ones correspond to a backscattered electron contrast.

This means that, with conventional L-PBF process, Fe_2VAl printed parts cannot be printed without defects.

A second approach was conducted and consisted in tuning the printing parameters starting from the ones provided for stainless steel. This part of the study led to the following conclusions :

1. With this approach, samples were successfully printed. Density measurement based on light micrographs showed density as high as 96.6%.
2. The transition from printed samples showing cold defects to printed samples showing overheating is rather fast. In between these two zones, there is a small process window where printing parameters are hot enough to ensure a sufficient cohesion of meltpools but cold enough to avoid overheating defects. This zone was called the "trade-off" zone.
3. At VED higher than 60 J/mm^3, strong warping defects start to appear. Above 80 J/mm^3, the warping defects are so large that the parts break and detach from the printing plate, in agreement with the conclusion of the SST approach.
4. In the "trade-off" zone, parameters used would produce SST in unmelting mode. Nevertheless, heat accumulation in a layer showed transition from unmelting to balling to continuous mode

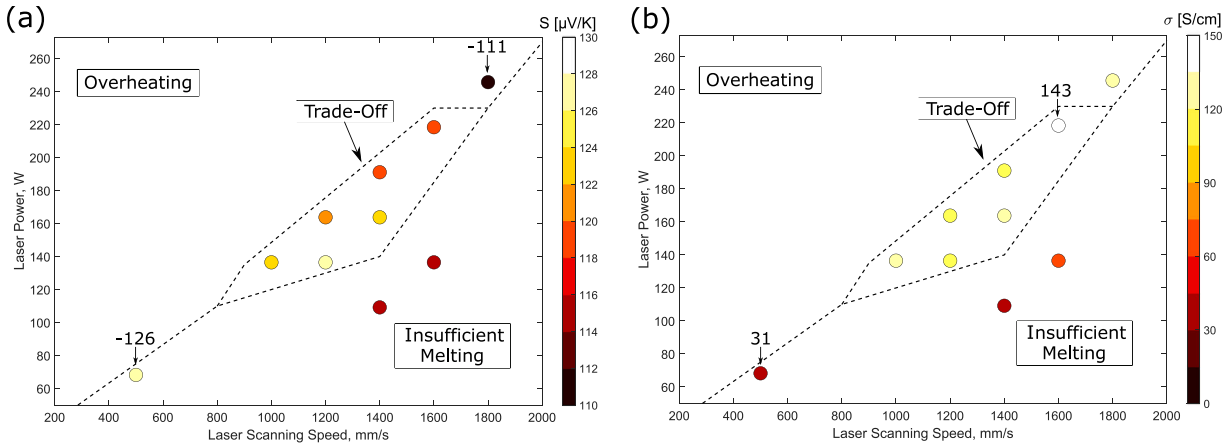

Fig. 8. Seebeck coefficient and electrical conductivity at 300 K of the printed samples. Details are available in Appendix.

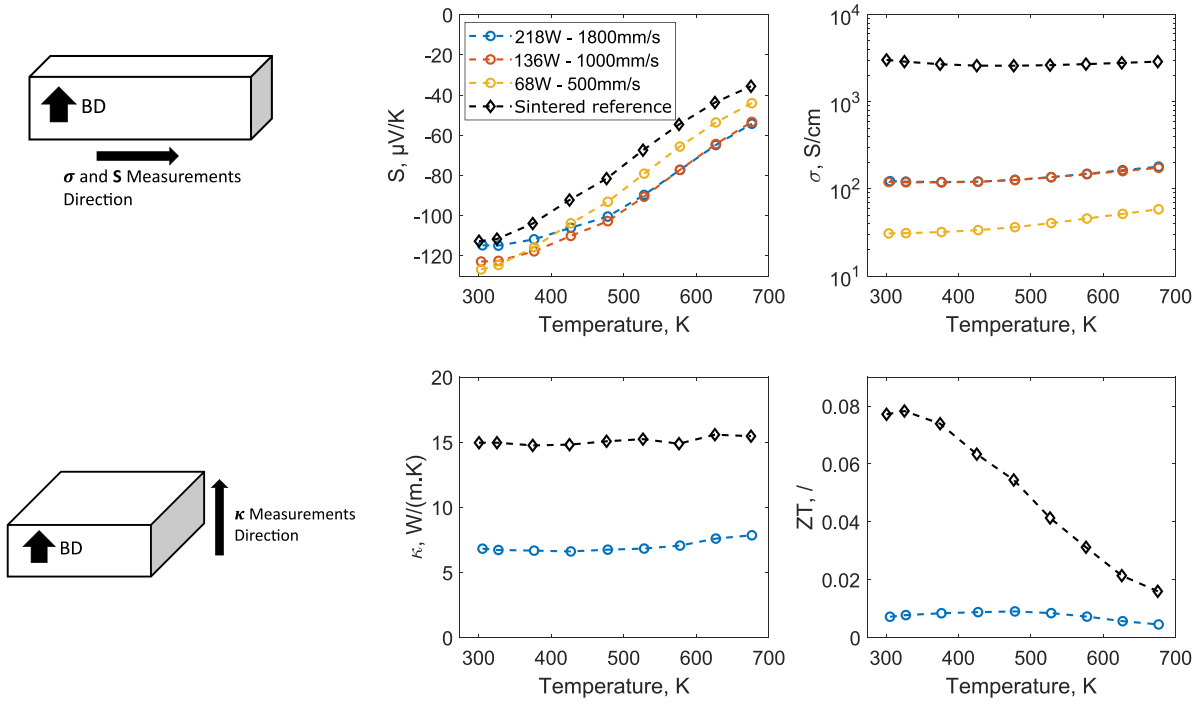

Fig. 9. Temperature dependence of the thermoelectric properties of printed samples compared to a sintered reference sample.

after several side by side laser scanning vectors, allowing to print bulk samples.

5. Scanning Electron Microscopy micrographs showed evidence of large numbers of transverse micro-cracks, parallel to the building direction. Lack-of-fusion defects were also observed, as expected from previous analysis.
6. The Seebeck coefficient measured on the printed samples was found to be fairly constant and close to the sintered reference sample. Nevertheless, the electrical conductivity of the printed sample in the "trade-off" zone was almost 2 orders of magnitude lower than the sintered reference sample. This is explained by the presence of a large amount of cracks.

To summarize, the feasibility of printing Fe_2VAl compounds by L-PBF was demonstrated although the printed parts show inherent defects such as lack-of-fusion or micro-cracks. Although these defects cannot be completely avoided with a conventional L-PBF process, there remains significant room for improving the quality of the printed parts. Future work should focus on strategies such as printing on a pre-heated build platform to reduce the thermal gradient between the solidifying melt pool and the substrate, thereby decreasing the cooling rate of the newly deposited layers and potentially mitigating crack formation. In parallel, post-print heat treatments (i.e. annealing or hot isostatic pressuring) should also be investigated to relieve internal stresses, promote $L2_1$ phase ordering in Fe_2VAl, heal cracks through diffusion mechanisms, and thus, potentially enhance thermoelectric performance of the printed parts.

Table 3
Synthesis of the process parameter set used for Approach II, along with the corresponding part quality and measured properties.

P [W]	v [mm/s]	HS [µm]	t [µm]	Ev [J/mm^3]	Zone	Appearance	σ [S/cm]	S [µV/K]	ρ_{rel} [%]
41	300	50	45	61	Inscufficient Melting	Detached	/	/	/
68	500	50	45	61	Inscufficient Melting	Slight defects (Low density)	31	−127	39.2
82	1200	50	45	30	Inscufficient Melting	Detached	/	/	/
109	1400	50	45	35	Inscufficient Melting	Slight defects (Low density)	40	−116	36.7
109	1600	50	45	30	Inscufficient Melting	Detached	/	/	/
136	1000	50	45	61	Trade-Off	Net-shape	120	−123	93.3
136	1200	50	45	51	Trade-Off	Net-shape	108	−127	76.8
136	1600	50	45	38	Inscufficient Melting	Slight defects (Low density)	66	−116	61.0
164	800	50	45	91	Overheating	Large defects (Warping edges)	/	/	/
164	1200	50	45	61	Trade-Off	Net-shape	109	−122	96.6
164	1400	50	45	52	Trade-Off	Net-shape	130	−122	92.6
191	600	50	45	142	Overheating	Detached	/	/	/
191	1000	50	45	85	Overheating	Large defects (Warping edges)	/	/	/
191	1400	50	45	61	Trade-Off	Net-shape	109	−119	96.3
218	800	50	45	121	Overheating	Detached	/	/	/
218	1200	50	45	81	Overheating	Large defects (Warping edges)	/	/	/
218	1600	50	45	61	Trade-Off	Net-shape	143	−119	91.8
246	1000	50	45	109	Overheating	Detached	/	/	/
246	1800	50	45	61	Overheating	Slight defects (Warping corners)	128	−111	97.3

CRediT authorship contribution statement

M. Delcroix: Writing – review & editing, Writing – original draft, Visualization, Validation, Methodology, Investigation, Formal analysis, Data curation, Conceptualization. **G. Roy:** Writing – review & editing, Conceptualization. **C. van der Rest:** Writing – review & editing, Conceptualization. **V. Marchal-Marchant:** Writing – review & editing, Conceptualization. **P.J. Jacques:** Writing – review & editing, Supervision, Conceptualization.

Declaration of competing interest

The authors declare that they have no known competing financial interests or personal relationships that could have appeared to influence the work reported in this paper.

Acknowledgments

M. Delcroix is a FRIA grantee of the Fonds de la Recherche Scientifique – FNRS and gratefully acknowledges their support. This work was also supported by the Walloon Region through the MultiMat3D project (Win2Wal n° 2010176).

Appendix. Parameter sets used for Approach II

See Table 3.

Data availability

Data will be made available on request.

References

[1] Yoichi Nishino, Thermoelectric properties of the pseudogap Fe2VAl system, Mater. Sci. Forum 449–452 (II) (2004) 909–912, http://dx.doi.org/10.4028/www.scientific.net/msf.449-452.909.

[2] F. Garmroudi, A. Riss, M. Parzer, N. Reumann, H. Müller, E. Bauer, S. Khmelevskyi, R. Podloucky, T. Mori, K. Tobita, Y. Katsura, K. Kimura, Boosting the thermoelectric performance of Fe2VAl-type Heusler compounds by band engineering, Phys. Rev. B 103 (8) (2021) 85202, http://dx.doi.org/10.1103/PhysRevB.103.085202.

[3] Kodai Fukuta, Koichi Tsuchiya, Hidetoshi Miyazaki, Yoichi Nishino, Improving thermoelectric performance of Fe2VAl-based Heusler compounds via high-pressure torsion, Appl. Phys. A: Mater. Sci. Process. 128 (3) (2022) 1–8, http://dx.doi.org/10.1007/s00339-022-05329-y.

[4] Fabian Garmroudi, Illia Serhiienko, Michael Parzer, Sanyukta Ghosh, Pawel Ziolkowski, Gregor Oppitz, Hieu Duy Nguyen, Cédric Bourgès, Yuya Hattori, Alexander Riss, Sebastian Steyrer, Gerda Rogl, Peter Rogl, Erhard Schafler, Naoyuki Kawamoto, Eckhard Müller, Ernst Bauer, Johannes de Boor, Takao Mori, Decoupled charge and heat transport for high-performance Fe$_2$VAl composite thermoelectrics, (ISSN: 20411723) 2024, pp. 1–9, arXiv:2410.07785.

[5] Onyebuchi Isreal Ibeagwu, Modelling and comprehensive analysis of TEGs with diverse variable leg geometry, Energy 180 (2019) 90–106, http://dx.doi.org/10.1016/j.energy.2019.05.088.

[6] Bengisu Şişik, Saniya LeBlanc, The Influence of Leg Shape on Thermoelectric Performance Under Constant Temperature and Heat Flux Boundary Conditions, Front. Mater. 7 (November) (2020) 1–13, http://dx.doi.org/10.3389/fmats.2020.595955.

[7] Christian Lundgaard, Ole Sigmund, A density-based topology optimization methodology for thermoelectric energy conversion problems, Struct. Multidiscip. Optim. 57 (4) (2018) 1427–1442, http://dx.doi.org/10.1007/s00158-018-1919-1.

[8] A. El-Desouky, A. L. Read, P. M. Bardet, M. Andre, S. LeBlanc, Selective laser melting of a bismuth telluride thermoelectric materials, in: Proc. Solid Free. Symp., 2015, pp. 1043–1050.

[9] Ahmed El-Desouky, Michael Carter, Matthieu A. Andre, Philippe M. Bardet, Saniya LeBlanc, Rapid processing and assembly of semiconductor thermoelectric materials for energy conversion devices, Mater. Lett. 185 (2016) 598–602, http://dx.doi.org/10.1016/j.matlet.2016.07.152.

[10] Yu Mao, Yonggao Yan, Keping Wu, Hongyao Xie, Zekun Xiu, Jihui Yang, Qingjie Zhang, Ctirad Uher, Xinfeng Tang, Non-equilibrium synthesis and characterization of n-type Bi2Te2.7Se0.3 thermoelectric material prepared by rapid laser melting and solidification, RSC Adv. 7 (35) (2017) 21439–21445, http://dx.doi.org/10.1039/c7ra02677c.

[11] Junhao Qiu, Yonggao Yan, Tingting Luo, Kechen Tang, Lei Yao, Jian Zhang, Min Zhang, Xianli Su, Gangjian Tan, Hongyao Xie, Mercouri G. Kanatzidis, Ctirad Uher, Xinfeng Tang, 3D Printing of highly textured bulk thermoelectric materials: Mechanically robust BiSbTe alloys with superior performance, Energy Environ. Sci. 12 (10) (2019) 3106–3117, http://dx.doi.org/10.1039/c9ee02044f.

[12] Yonggao Yan, Hongquan Ke, Jihui Yang, Ctirad Uher, Xinfeng Tang, Fabrication and Thermoelectric Properties of n-Type CoSb2.85Te0.15 Using Selective Laser Melting, ACS Appl. Mater. Interfaces 10 (16) (2018) 13669–13674, http://dx.doi.org/10.1021/acsami.8b01564.

[13] Yonggao Yan, Wuqian Geng, Junhao Qiu, Hongquan Ke, Chuang Luo, Jihui Yang, Ctirad Uher, Xinfeng Tang, Thermoelectric properties of n-type ZrNiSn prepared by rapid non-equilibrium laser processing, RSC Adv. 8 (28) (2018) 15796–15803, http://dx.doi.org/10.1039/c8ra00992a.

[14] Maxime Baudry, Guillaume Savelli, Guilhem Roux, 3D printing of bulk thermoelectric materials: Laser powder bed fusion of N-type silicon germanium, Mater. Sci. Eng.: B 298 (August) (2023) 116897, http://dx.doi.org/10.1016/j.mseb.2023.116897.

[15] Leonie Gomell, Moritz Roscher, Hanna Bishara, Eric A. Jägle, Christina Scheu, Baptiste Gault, Properties and influence of microstructure and crystal defects in Fe2VAl modified by laser surface remelting, Scr. Mater. 193 (2021) 153–157, http://dx.doi.org/10.1016/j.scriptamat.2020.10.050.

[16] Leonie Gomell, Tobias Haeger, Moritz Roscher, Hanna Bishara, Ralf Heiderhoff, Thomas Riedl, Christina Scheu, Baptiste Gault, Microstructure manipulation by laser-surface remelting of a full-Heusler compound to enhance thermoelectric properties, Acta Mater. 223 (2022) 117501, http://dx.doi.org/10.1016/j.actamat.2021.117501.

[17] I. Yadroitsev, I. Yadroitsava, A. Du Plessis, E. MacDonald, Fundamentals of Laser Powder Bed Fusion of Metals, Elsevier, 2021.
[18] Changchun Zhang, Tingting Liu, Wenhe Liao, Huiliang Wei, Ling Zhang, Investigation of the Laser Powder Bed Fusion Process of Ti-6.5Al-3.5Mo-1.5Zr-0.3Si Alloy, Chin. J. Mech. Eng. (Engl. Edition) 36 (1) (2023) http://dx.doi.org/10.1186/s10033-023-00863-z.
[19] Morgan Letenneur, Alena Kreitcberg, Vladimir Brailovski, Optimization of laser powder bed fusion processing using a combination of melt pool modeling and design of experiment approaches: Density control, J. Manuf. Mater. Process. 3 (1) (2019) http://dx.doi.org/10.3390/jmmp3010021.
[20] Julie Gheysen, Matthieu Marteleur, Camille van der Rest, Aude Simar, Efficient optimization methodology for laser powder bed fusion parameters to manufacture dense and mechanically sound parts validated on AlSi12 alloy, Mater. Des. 199 (2021) 109433, http://dx.doi.org/10.1016/j.matdes.2020.109433.
[21] G. Roy, C. Van Der Rest, S. Heymans, E. Quintin, V. Dupont, J.P. Erauw, A. Schmitz, P.J. Jacques, Global Analysis of Influence of Contacts on Heusler-Based Thermoelectric Modules, J. Electron. Mater. 48 (9) (2019) 5390–5402, http://dx.doi.org/10.1007/s11664-019-07137-2.
[22] M. Mikami, M. Mizoshiri, K. Ozaki, H. Takazawa, A. Yamamoto, Y. Terazawa, T. Takeuchi, Evaluation of the thermoelectric module consisting of W-doped heusler Fe2VAl alloy, J. Electron. Mater. 43 (6) (2014) 1922–1926, http://dx.doi.org/10.1007/s11664-013-2910-7.
[23] Ali Eliasu, Aleksander Czekanski, Solomon Boakye-Yiadom, Effect of laser powder bed fusion parameters on the microstructural evolution and hardness of 316L stainless steel, Int. J. Adv. Manuf. Technol. 113 (9–10) (2021) 2651–2669, http://dx.doi.org/10.1007/s00170-021-06818-9.
[24] Seulbi Lee, Jaewoong Kim, Jungho Choe, Seong Woong Kim, Jae Keun Hong, Yoon Suk Choi, Understanding Crack Formation Mechanisms of Ti–48Al–2Cr–2Nb Single Tracks During Laser Powder Bed Fusion, Met. Mater. Int. 27 (1) (2020) 78–91, http://dx.doi.org/10.1007/s12540-020-00770-1.
[25] Eva Ostertagová, Oskar Ostertag, Methodology and Application of Oneway ANOVA, Am. J. Mech. Eng. 1 (7) (2013) 256–261, http://dx.doi.org/10.12691/ajme-1-7-21.
[26] E. Liverani, S. Toschi, L. Ceschini, A. Fortunato, Effect of selective laser melting (SLM) process parameters on microstructure and mechanical properties of 316L austenitic stainless steel, J. Mater. Process. Technol. 249 (May) (2017) 255–263, http://dx.doi.org/10.1016/j.jmatprotec.2017.05.042.
[27] Y. Nishino, H. Kato, M. Kato, U. Mizutani, Effect of off-stoichiometry on the transport properties of the Heusler-type (formula presented) compound, Phys. Rev. B - Condens. Matter Mater. Phys. 63 (23) (2001) 3–6, http://dx.doi.org/10.1103/PhysRevB.63.233303.